ORIGINAL ARTICLE

A Laser-Micromachined PCB Electrolytic Micropump Using an Oil-Based Electrolyte Separation Barrier

Seonhyeok Baek[1] · Hakhyun Kim[1] · Heewon Hwang[1] · Abdi Mirgissa Kaba[1] · Hyeonsik Kim[2] · Minsub Chung[3] · Jintae Kim[2] · Dohyun Kim[1]

Abstract

We report a laser-micromachined electrolytic PCB micropump with an oil separation barrier. As advances in terms of miniaturization and performance from our previous mesoscale PCB electrolytic pump (Kim et al. in Sens Actuators A Phys 277:73–84, 2018), we employed a simple yet rapid tape-based laser-machining technique called tape-liner-supported plastic laser micromachining and pattern transfer to fabricate a microfluidic coverslip for a PCB electrode chip. Using our microfabrication technique, the coverslip is bonded to a PCB chip to form an enclosed microscale pump with a high machining precision and no need for alignment of intermediate adhesive tapes with structural layers as commonly done in previous tape-bonding work. The completed micropump demonstrated excellent pumping performance: flow rate up to 24.49 ml/min and backpressure up to 394 kPa. Electrochemical activation of electrodes consisting of a train of voltage pulses and sweeps improves the pumping performance. In order to prevent unwanted interspersion between the electrolyte and working fluid, various separation diaphragms were previously employed, but at the cost of limited working volume and flow rate as the diaphragms were permanently anchored to the pump body. Here we propose to use an oil plug as an untethered (mobile) separation barrier. After a systematic study of properties of common oils, we tested fluorinated oil (HFE-7500), hexadecane, and tetradecane as the candidate barrier materials. HFE-7500 was chosen because its interface was stable and did not degrade pumping performance for the flow-rate range of 8.47 μl/min–2.48 ml/min. We expect our micropump with the oil plug to be used as an excellent pressure source for integrated lab-on-a-chip devices, especially lab-on-a-PCBs.

Keywords Electrolytic micropump · Printed circuit board (PCB) · Laser machining · Pressure-sensitive tape · Immiscible phases · Fluorinated oil

1 Introduction

There have been significant efforts to develop self-contained, microscale, active micropumps because of wide applications in various fields including μTAS (micro-total-analysis-systems), biomedical microdevices (e.g., insulin pump), microelectronics, and microhydraulics [1–7]. Among these applications, the μTAS has received tremendous attention recently owing to the rapid and accurate determination of bio-/chemical analytes of a minuscule quantity in a small form factor. In order to handle reagents and samples on a pico- to microliter scale in a swift and controlled manner, a reliable and miniaturized pressure source, i.e., micropump, is crucial. Many μTAS still rely on external pumps (e.g., syringe pump) or pressure tanks (e.g., air or nitrogen), which are heavy, and consume much power and occupy ample space. Therefore, an integrable micropump with a high flow rate, excellent backpressure, and small power consumption may be a key to a wide success of the μTAS, especially portable systems such as POC (point-of-care) devices.

Previously we reported a PCB (printed circuit board)-based electrolytic pump. The PCB pump was compared with a microfabricated counterpart (photolithographically defined gold electrodes on a glass substrate), in terms of

✉ Dohyun Kim
  dohyun.kim@mju.ac.kr

[1] Department of Mechanical Engineering, Myongji University, 116 Myongji-Ro, Yongin 17058, Republic of Korea

[2] Department of Electrical and Electronics Engineering, Konkuk University, Gwangjin-Gu, Seoul 05029, Republic of Korea

[3] Department of Chemical Engineering, Hongik University, Mapo-Gu, Seoul 04066, Republic of Korea

performance metrics, including power consumption, lifetime, flow rate, and cost [8]. As the pumping mechanism, we opted for electrolysis, the phase change of water into hydrogen and oxygen gases through electrolysis reaction, because of extraordinary volume expansion (×1360) and pressure (up to 200 MPa), high efficiency, and low power consumption [9–11]. In addition, an electrolytic pump is simple to construct because only an electrolyte and a pair of electrodes are required without moving parts. It is also easy to operate as a constant (dc) current is sufficient to control flow rate. In contrast to our previous work [8], here we employ electrochemical activation of electrodes consisting of multiple voltage pulses and sweeps to reduce overpotential and improve pumping performance because fresh gold electrodes on a PCB chip could not effectively generate flow due to electrochemical inactivity [12–15].

The PCB technology was employed in our previous micropump [8]. As demonstrated in PCB-based microanalytical systems (so-called Lab-on-PCB) [16–19], the PCB has the potential to be an effective microanalytical platform technology owing to versatility, scalability, the capability to incorporate various electrical and electromechanical components (e.g., solenoid valve, logic circuits, control IC, sensors, microprocessors, communication IC), easy fabrication based on well-standardized foundry services, and manufacturing accuracy (~ 100 μm) suitable for microfluidic systems [20–22]. We fabricated a PCB chip with the interdigitated (IDT) gold electrodes using a local PCB foundry service. Our PCB chip was better than the microfabricated counterpart, which had the same electrode geometry, regarding the various pumping-performance metrics [8]. We developed our PCB micropump to be used in a future PCB-based multitarget microanalytical system integrated with a CMOS biosensor array and fluidic components [23].

We employed conventional machining, i.e., drilling and milling, to construct a PMMA [poly(methyl methacrylate)] microfluidic cartridge (i.e., housing) for the previous PCB micropump [8]. Although noticeably high backpressure (up to 547 kPa) was obtained, it was cumbersome to machine the PMMA parts and assemble the cartridge using screws and nuts. Most of all, this mesoscale cartridge is too copious to be used in a μTAS. Thus, in this report, we seek to construct a "true" microfluidic pump by employing laser cutting as a straightforward yet reliable micromachining technique.

Indirect replication techniques, including hot embossing [24, 25], injection molding [26, 27] and casting [28], or direct machining techniques, including laser ablation [29, 30], milling [31, 32], cutting plotter [33], 3D printing [34–36], high-aspect-ratio photoresist [37] and surface micromachining [38], have been used for polymer microfabrication [39, 40]. We opted for CO_2 laser machining to fabricate a PMMA-microfluidic coverslip (i.e., cartridge) because a relatively high-resolution cutting down to 44 μm

can be made on thermoplastics without a cleanroom [41, 42]. Replication techniques (i.e., SU-8-based master-mold production) and some direct techniques (i.e., high-aspect-ratio photoresist and surface micromachining) still rely on photolithography. Thus, even a small design modification may cause cost and time increases due to costly lithographic processes [43]. In contrast, rapid prototyping based on laser ablation enables facile design iterations because it takes tens of minutes to a few hours from a CAD design to a complete chip [44, 45]. A setup cost of a high-precision CO_2 laser cutter is just in the order of a few tens of thousand dollars, and the material and running costs are relatively cheap, compared to the other polymer microfabrication techniques. Also, it does not require extensive user training, unlike the cleanroom-based microfabrication methods. Compared to other direct techniques, it would not leave rough surfaces and burrs as in milling and drilling [31] or voxel patterns and opaque surfaces in 3D printing [35, 46, 47] that may hinder optical measurement and cause trapping of bubbles and biomolecules.

Among the two types of laser machining modes, engraving and cutting, here we rely on cutting because engraving yields Gaussian-shaped cross-sections [45, 48] and leaves rough "raked" bottom surfaces that may hinder visual observation [49]. Our approach is first to cut microfluidic features such as chambers and channels in a thin PMMA sheet to yield a cut-through layer with practically vertical sidewalls. Then the cut-through layer is sandwiched between a PCB electrode chip and a PMMA layer with fluidic interfaces. In this way, microfluidic features with vertical sidewalls and smooth inner surfaces (especially top and bottom) are ensured. Thermal fusion bonding tends to distort microfluidic features, be sensitive to surface cleanness, and requires substantial process optimization [50]. Solvent bonding requires toxic solvents and also tends to deform the microfeatures and clog channels [51, 52]. Instead, we opted for innocuous adhesive bonding using a thin industry-grade pressure-sensitive transfer tape. Moreover, a PCB, the base layer of our micropump, is dissimilar to the PMMA layer; a PCB has a soldermask (lacquer-like surface) on an FR-4 composite sheet. Therefore, it appears that adhesive bonding is suitable to bond a PCB chip and a PMMA coverslip of heterogeneous surfaces. To minimize nonspecific adsorption of biomolecules on exposed tape in sidewalls [53], we employed a thin transfer tape (50 μm) [44, 54].

As an advance in rapid polymer microfabrication compatible with a PCB platform, we devised a novel laser ablation and bonding technique called Tapes-liner-supported Plastic Laser Micromachining and Pattern Transfer (TPLMPT). Before cutting to form microfluidic features, the top and bottom of the PMMA sheet were pre-pasted with the transfer tapes. In this way, microfluidic features were formed on a tape-PMMA-tape composite sheet.

Thus, without a need for cumbersome alignment between a micro-patterned PMMA and an adhesive tape of the same patterns, the PCB chip and coverslip were directly bonded to the pre-machined composite layer, simplifying the assembly process to a great extent [55]. A drawback of this approach could be that the composite layer becomes significantly flimsy, especially when the layer is thin, and has a long and complex microchannel network. Therefore, a notable dimensional change can occur during bonding. A key idea of our TPLMPT technique is that a few layers of additional protective tapes were pasted onto the bottom of the composite layer as a mechanical support. Laser cutting parameters are optimized so that the protective tapes are not be fully penetrated. The uncut protective tapes (total thickness of ~ 830 μm) mechanically support the flimsy composite layer. Therefore, the microfluidic features can be transferred to the PCB chip with minimal dimensional alteration, compared to the case where the composite layer is penetrated. After the bonding was finished, flow-generation and backpressure performances of the completed micropump were characterized [8].

Although the electrolytic pump essentially is electrolyte and electrodes in a container with a nozzle, gas-generating electrolyte should be separated from working fluid (typically buffer solution, reagents, or biological samples) to prevent cross-contamination, which is of particular importance for biological and chemical analyses. In early demonstrations of the electrolytic pumps, the reagent or the sample itself had been used as an electrolyte [56–58], causing significant contamination. Later, the electrolysis chamber was separated from the sample or reagent chamber using a flexible diaphragm made of silicone rubber [59, 60], PDMS [61–63], parylene [64, 65], and nitrile rubber [66]. However, regardless of flexibility, the periphery of the diaphragm was permanently anchored to the pump body, inevitably limiting working volume, and deteriorating flow rate and pressure performances. An air bubble between two vertically separated reservoirs [67] and an air bubble on a hydrophobic surface were suggested as alternative separation barriers [68]. However, air bubbles may not have long-term stability (e.g., dissolving into neighboring liquid plugs). As a novel yet simple remedy for the cross-contamination problem, we *for the first time* employ an oil plug for effective isolation of the aqueous electrolyte and working fluid because they are immiscible. After comparing a handful of common low-viscosity oils (i.e., mineral oils, fluorinated oils, hexadecane, and tetradecane), candidate oils with favorable physicochemical properties were selected as a barrier material. The best oil was chosen after pumping experiments were conducted to test barrier stability (i.e., immiscibility) and influence on flow rate under various flow conditions.

2 Theory

2.1 Electrolytic Pumping

Electrolysis occurs when a voltage, higher than the standard equilibrium voltage of water electrolysis, is applied to an electrode pair in an aqueous solution. Reduction takes place at a cathode by donating four electrons to four H^+ ions to form two H_2 gas molecules. At an anode, oxidation occurs by accepting four electrons from two H_2O molecules to generate one O_2 gas molecule. The produced gases yield an extraordinary volume expansion of 1350× greater than the consumed liquid volume and theoretical pressure generation up to 200 MPa. This significant volume expansion and high pressure caught attention as an effective means to generate flow [9].

Assuming that the applied current contributes 100% to the electrolysis reaction, and no gases are leaked, the flow rate Q [m^3/s] generated by a constant current I [A] is equivalent to the rate of electrolytic gas production:

$$Q = \frac{3V_m}{4F}I, \tag{1}$$

where V_m is the molar gas volume (24.7×10^{-3} m^3/mol at 1 atm, 25 °C), and F is the faraday constant (96,485 C/mol). Consequently, the flow rate Q is proportional to the current I. According to Eq. (1) the flow rate is estimated as ~ 10 μL/min (1 atm) when the current is 1 mA, adequate for typical LOC applications [69].

2.2 Minimizing Power Consumption

It is important to minimize the power consumption of an integrated micropump for portable μTAS applications such as a multi-target CMOS microanalytical system [70]. For constant current mode, consumed power P_{cell} is proportional to the electrolysis cell voltage V_{cell}. Previously we proposed a first-degree approach to minimize V_{cell}, assuming that (1) the activation overvoltage V_{act} is predetermined because the electroplated gold film was chosen as the electrode material (i.e., metal used in a standard PCB manufacturing technology), (2) the major contributing factor to V_{cell} is Ohmic overvoltage V_{ohm}, and (3) the cell resistance R_{cell} contributes the most to the Ohmic overvoltage among other resistances. Interdigitated (IDT) electrode design was selected due to low R_{cell}. For a fixed electrode footprint (9.4×9.4 mm^2), two design parameters of the IDT electrode, W the width of a finger and S the space between two fingers, were theoretically optimized to have the lowest R_{cell} using the formula proposed by Olthuis et al. [71]. Our optimization study suggested that the smallest W and S achievable with the PCB

manufacturing technology yield minimal R_{cell}. Consequently, $W = 100$ μm and $S = 100$ μm were chosen. We also experimentally verified the theory by measuring power consumption and flow rate generated with varying W and S values. For more detail, the readers are directed to our previous work [8].

2.3 Electrode Material Selection

Two types of gold coatings on copper traces are available in a standard PCB manufacturing process. Electroless Nickel Immersion Gold (ENIG) layer is formed by displacing nickel atoms electroplated on the copper with gold atoms. Hard gold is an electroplated gold layer on the copper using a nickel adhesion layer. ENIG was much thinner (~0.04 μm) than hard gold (~0.43 μm). As a result, the ENIG was easily damaged during electrolysis [8]. Flow generation performance was better for hard gold in identical electrolysis conditions. In addition, similar power consumption and manufacturing accuracy were observed for both gold materials. Therefore, we chose hard gold as the electrode material.

2.4 Oil Separation Barrier

In an electrolytic pump, electrolyte solution should be isolated from working fluid (e.g., buffer, reagents, biological or chemical samples) to prevent interspersion. Cross-contamination is a critical problem for biological and chemical analyses, which are common applications of μTAS. In many previous micropumps, the electrolyte was separated from the working fluid using a flexible diaphragm including silicone rubber, PDMS, and parylene, as illustrated in Fig. 1a. The diaphragm deflects upon pressure generation when current is applied to the electrode for electrolysis. Then the diaphragm pushes the working fluid to create flow. However, flow- and pressure-generation performances are deteriorated because the diaphragm is permanently anchored to the pump body. Furthermore, working volume (i.e., a maximum liquid volume that can be pumped) is limited. Therefore, we propose an unanchored oil plug as a novel separation barrier.

In the macroscale, oil and water are separated by a horizontal interface because of their immiscibility and the difference in density. On the other hand, surface tension can overcome gravitation on microscale, and thus a vertical interface can form between the two immiscible liquids [72]. A stable, vertical interface between oil and water has often been exploited in microfluidics including droplet microfluidics [73], protein crystallization [74], and microsphere fabrication [75]. Noting this interesting property of immiscible microscale interfaces, we attempted to use an oil plug for the isolation of the electrolyte, as depicted in Fig. 1b.

An oil plug, if chosen carefully, can form stable and mobile immiscible interfaces with working fluid and
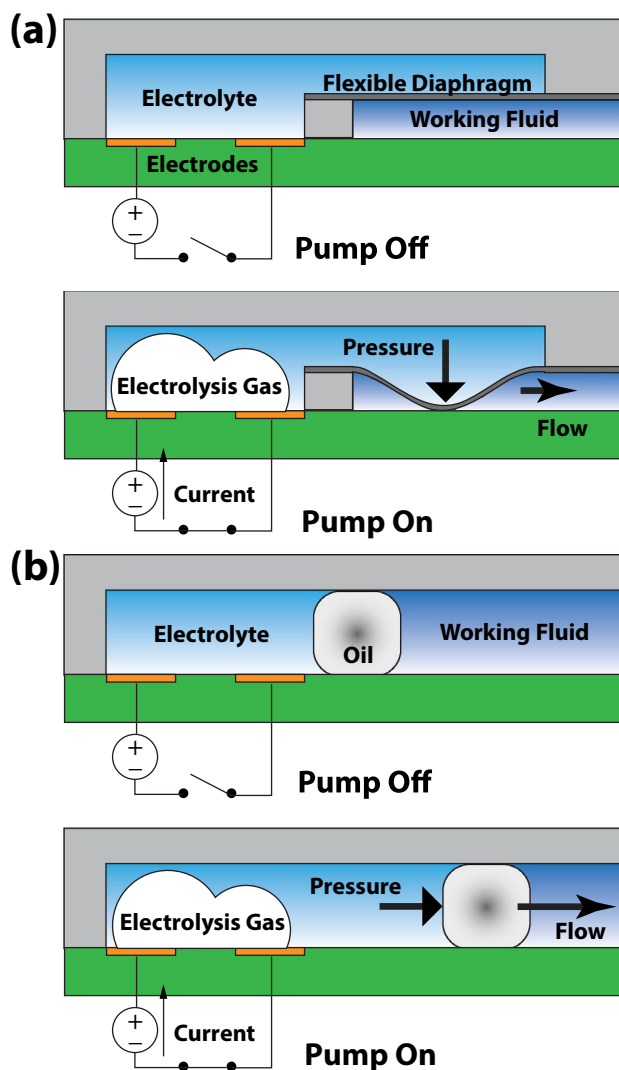

Fig. 1 Working principles of **a** a conventional electrolytic micropump with a tethered flexible diaphragm separating the electrolyte and working fluid and **b** our micropump relying on an unanchored oil plug flowing with immiscible electrolyte and working fluid

electrolyte. When pressure is generated due to electrolysis, the oil plug can flow with the two neighboring liquids as concatenated plugs while preventing interspersion between the two liquids. Air bubbles were previously used for this purpose [67, 68]. However, long-term stability was a problem (e.g., air dissolution into neighboring aqueous solutions and interface breakage under vibration) as the pump-integrated μTAS should be stored for a long time. For plug materials, we investigated a handful of oils commonly used in microfluidics. The criteria were (1) low viscosity for reduced backpressure, (2) low vapor pressure for long-term storage, (3) high flashpoint for fire safety, and lastly (4) material compatibility with PMMA. The properties of candidate oils, namely fluorinated oil (HFE-7500, 3M, Maplewood, USA), hexadecane (Tokyo Chemical Industry,

Tokyo, Japan), tetradecane (Sigma, St. Louis, MO, USA), and light mineral oil (Sigma), are listed in Table 1 with water as a reference. First, the oils of low viscosities were tested in our micropump to see if the water–oil-water immiscible phases remained stable, and cross-contamination between electrolyte and working fluid occurred at various flow rates. Second, we tested if a plug reduces flow rate compared to the control cases where a plug is not present.

3 Design and Fabrication of Micropumps

3.1 Design of the PCB Electrode Chip

The detailed design and fabrication processes for the PCB chip (Fig. 2a) are elsewhere [8]. Briefly, we chose both width W and spacing S of IDT electrode fingers as 100 μm, because 100 μm is the minimum feature size afforded by a local PCB manufacturing service (Hansaem Digitec, Incheon, South Korea), and the power consumption can be minimized as described in Sect. 2.2. The total electrode surface area was 35.88 mm^2 (46 fingers). The footprint of the IDT electrode was chosen as 9.4×9.4 mm^2, considering the size of the electrolysis chamber (Fig. 2b). The size of the PCB chip was the same as that of a standard glass slide (2.5×7.5 cm^2). The feedlines electrically link the electrodes to the bonding pads, which are then connected to a source meter. A 0.35-μm gold and a 5.47-μm nickel adhesion layer were electroplated on copper traces to form hard-gold electrodes. The total height of the electrode sidewall was 24.39 μm (all measurements are conducted by Kigang electronics, Incheon, South Korea). Having such a high sidewall (compared to that of microfabricated counterparts, typically less than 1 μm [8]) and catalytic activities on water electrolysis (nickel [85] and copper [86]), the PCB electrode sidewall may improve electrolysis and thus pumping performance, compared with microfabricated counterparts.

3.2 Design of the Microfluidic Coverslip

The micropump consists of three layers: a bottom PCB chip, an intermediate microfluidic layer, and a top layer (Fig. 2c). The microfluidic layer and the top layer constitute a microfluidic coverslip. The microfluidic layer was formed by laser micromachining of a 1-mm thick PMMA sheet, which contains microfluidic features such as an electrolysis chamber and a serpentine microchannel (Fig. 2c). The serpentine design was chosen to maximize the channel length for a given chip footprint (i.e., standard glass-slide format). The length and width of the electrolysis chamber are 35.13 and 10.0 mm, respectively, and the volume of the chamber is 243 μl. The electrolysis chamber has a tapered (42°) inlet and outlet for smooth transitions of flow in and out. The outlet of the chamber is connected to a serpentine microchannel of dimension $L \times W \times H = 175.9 \times 0.5 \times 1.0$ mm^3 (88 μl). The microchannel is used as a storage and a conduit for an oil plug and working fluid. For flow rate and backpressure measurement, only electrolyte was loaded into the chamber and microchannel. For the characterization of oil separation barriers, an electrolyte was injected into the chamber, followed by an oil plug and a working fluid into the channel. Five fiducials (the distance between two nearby fiducials = 44.8 mm) were patterned near the microchannel and used for optical flow-rate measurement. The stability and flow rate of concatenated liquid segment (i.e., electrolyte—oil plug—working fluid) were also optically characterized.

The top layer has two 1.6-mm-diameter holes, one for the inlet to the electrolysis chamber and the other for the outlet from the microchannel. For quick coupling and decoupling of tubing, Luer Lok fluidic ports were bonded to the layer after aligning them to the hole centers. The microfluidic layer and top layer were pre-bonded to form a microfluidic coverslip. The photograph of an assembled PCB micropump is shown in Fig. 2d.

Table 1 Physical properties of candidate oils for the separation barrier (at 25 °C, except flash point). Properties of water are also tabulated as a reference

	Viscosity (cP)	Vapor pressure (mmHg)	Density (g/cm^3)	Flash point (°C)	PMMA compatibility
Fluorinated oil (HFE-7500)	0.77 [76]	15.75 [76]	1.610 [76]	Non-flammable [76]	Resistant [76]
Hexadecane	3.00 [77]	1.5×10^{-3} [78]	0.770 [78]	136 ℃ [78]	Resistant [79]
Tetradecane	2.13 [80]	15×10^{-2} [80]	0.767 [80]	100 ℃ [80]	Resistant [79]
Mineral Oil	$> 17.1^a$ [81]	$^b7.5 \times 10^{-5}$ [81]	0.833 [81]	> 112 ℃ [81]	Resistant [82]
Water	0.895 [83]	23.8 [84]	0.997 [83]	Non-flammable	Resistant [82]

[a]Measured at 40 °C, and therefore the viscosity should be higher at 25 °C
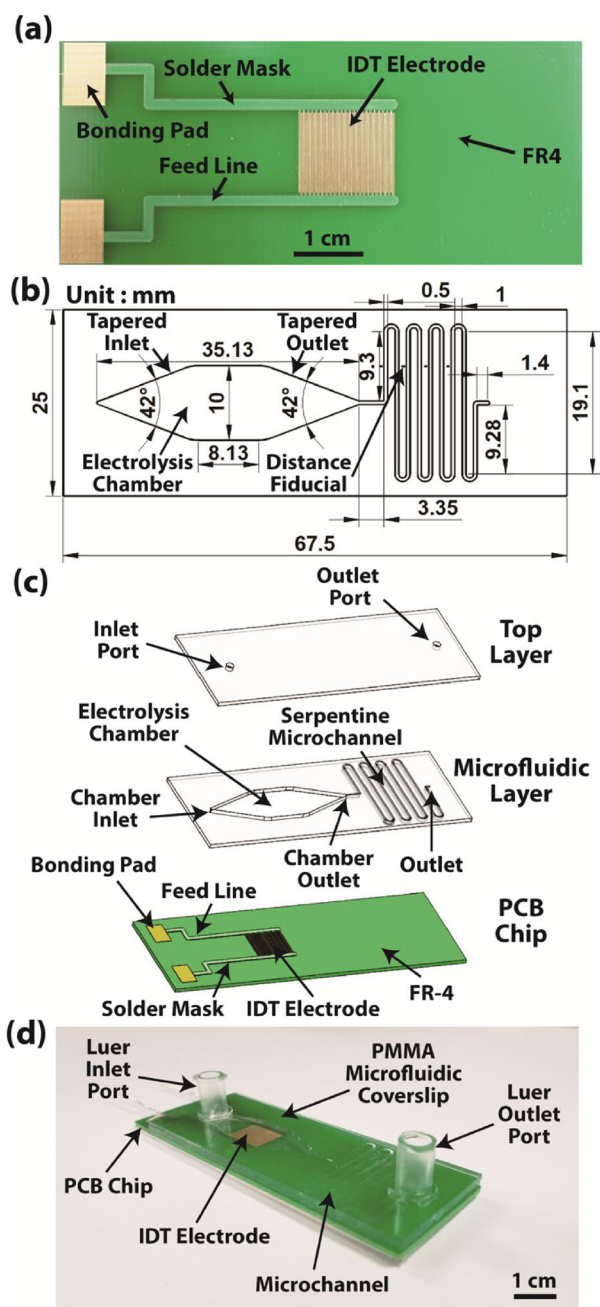
[b]Measured at 20 °C

Fig. 2 Design of the microfluidic pump. **a** The photograph of a PCB electrode chip in a glass-slide format (25 mm × 75 mm) with electroplated hard gold interdigitated electrode (width = 100 µm, spacing = 100 µm, and surface area = 35.88 mm²). **b** The detailed design of the microfluidic layer, housing an electrolysis chamber and a serpentine microchannel. **c** Exploded view of the pump, consisting of the top layer with fluidic interfaces, the intermediate microfluidic layer, and the bottom PCB electrode chip. **d** The photograph of a completed microfluidic pump

3.3 Tape-Supported Laser Micromachining of the Microfluidic Chip

CO_2 laser cutting is a contactless, subtractive process that can machine optically transparent thermoplastics including PMMA and PC (polycarbonate) [87]. During the interaction with a laser beam, the absorbed energy converts into heat in a short period of time. Confinement of heat to a localized region results in melting followed by vaporization (i.e., ablation). It was reported that cutting results on the PMMA sheet mainly depend on the power and frequency of a laser source and the speed of the beam spot [48]. To avoid the use of potentially toxic solvents for bonding (i.e., solvent-assisted bonding [51, 87]) and to bond two heterogeneous surfaces (i.e., between PMMA and PCB), we opted for adhesive bonding based on pressure-sensitive adhesive (PSA) [88]. By combining laser cutting and adhesive bonding, we developed TPLMPT (Tapes-liner-supported Plastic Laser Micromachining and Pattern Transfer) process. The TPLMPT is a simple yet reliable method of transferring microfluidic patterns to a PMMA substrate.

3.3.1 General Effects of Laser-Machining Parameters on Cutting Quality

We investigated general effects of laser-machining parameters, namely S (speed, %), P (power, %), and F (frequency, Hz), on cutting quality i.e., kerf width, surface roughness, and contouring error before an optimization of laser cutting. A tape-PMMA-tape composite sheet was cut using a 50-W CO_2 laser machine (Mini 24, Epilog, Golden, CO, USA). For the composite sheet, a 1-mm-thick PMMA sheet (Acryl Choi-ga, Seoul, Korea) was pre-pasted with transfer tapes 467MP (3M), consisting of 60 µm-thick adhesive and 110 µm-thick polyethylene-coated kraft paper (PCK) liner, on both sides. Here we seek to qualitatively assess cutting quality using a microscope (BX-40, Olympus, Tokyo, Japan) because rigorous characterization requires dedicated instruments (e.g., surface profilometer) with substantial efforts, which is beyond the focus of this study. The general observation was as follows: (1) a reduction in kerf width and increase in surface roughness and contouring error were observed with increasing S; (2) surface roughness decreased, and kerf width increased with no significant change in contouring error with increasing P; (3) finally, an increase in F resulted in decreases in both surface roughness and kerf width. The detailed procedure of studying the effects of laser cutting is provided in Section S1 of SI (Supplementary Information).

3.3.2 Experimental Optimization of the Laser Cutting Parameters

After noting the general effects of the cutting parameters on the machining quality, an experimental optimization of the best cutting parameter set (S, P, F) for the composite sheets was performed. The optimization objective was to yield the microfluidic features (Fig. 2b) with a smooth channel sidewall, small kerf width, and minimal contouring error. A stepwise exhaustive search for (1) excellent surface roughness (Fig. S1a in SI), (2) minimal kerf width, and (3) small contouring error (Fig. S1b in SI) was performed in the parameter space of $S = 1$–7%, $P = 1$–7%, and $F = 5000$ Hz with some constraints (e.g., no penetration of the bottommost tape). The optimal laser machining parameter was determined to be $P = 5\%$, $S = 3\%$, and $F = 5000$ Hz. The detailed optimization procedure is given in Section S2 of SI.

3.3.3 Micropump Fabrication Using the TPLMPT Process

After obtaining the best cutting parameter set, the TPLMPT was performed for micropump fabrication. The process comprises the following three steps (Fig. 3):

Step 1: a 1-mm-thick PMMA is cut through to form inlet and outlet holes (1.8-mm diameter). Debris from laser ablation is cleaned using compressed nitrogen gas to prepare a top layer.

Step 2: To form a composite intermediate layer, a 1 mm-thick PMMA sheet is pre-pasted with transfer tape 467MP on both top and bottom. Then an additional stack (3 layers) of transfer tapes 468MP (3M), having 130 μm-thick adhesive and 110 μm-thick PCK liner, is attached to the liner of the bottom transfer tape (the same PCK liner). A major role of the PCK liner is to release the adhesive material without residue and also to provide mechanical support to thin adhesive [89]. The polyethylene coating of the kraft-paper liner provides thermal stability, tear resistance, and puncture resistance. Therefore, the stack of the PCK liner and adhesives survived laser ablation and provided a certain level of rigidity to support the flimsy cut layer of 1-mm PMMA. In this way, microfluidic features were transferred to the PCB chip with an excellent dimensional integrity. We also tested other tapes, laboratory masking tape (40 μm-thick rubber adhesive and 100 μm Crepe paper, 3M) and industry-grade kraft tape (30 μm-thick rubber adhesive and 110 μm-thick PCK liner; Sekisui Chemical, Tokyo, Japan). However, significant yellow discoloring of PMMA was observed after laser cutting. Moreover, 6 to 8 layers must be stacked to prevent penetration, which may render the TPLMPT process cumbersome, compared to the process using only three 486 MP layers. As a result, we chose the 468 MP as the protective tape. The composite layer (i.e., 467MP + PMMA + 467MP + three 468MPs) was pressurized for strong bonding using an artist roller. The layer was laser-cut, but the bottom protective-tape stack (a total of 873 μm) was not fully penetrated (the bottommost liner usually remained intact) when using the optimized laser cutting parameters. Non-zero kerf width was considered in the microfluidic layer design (Fig. 2b). For example, the design was adjusted to have a 300 μm channel width and 1200 μm channel pitch if the measured kerf width was 200 μm. After cleaning the debris, the top tape liner was removed to expose the underlying adhesive.

Step 3: After a brief manual alignment, the microfluidic layer prepared in **Step 2** was bonded to the top layer using the roller to form a microfluidic coverslip. Manual alignment between the top and the microfluidic layer was straightforward because of ample clearance (e.g., inlet and outlet hole sizes = 1.8 mm, channel width = 500 μm). After the bonding was completed, the bottom tape liner along with the protective tape stack was peeled off to expose the underlying adhesive. The microfluidic coverslip with the exposed adhesive was then bonded to the PCB chip to enclose microfluidic features. Finally, Luer Lok fluidic ports (09–0512-0303–01, Microfluidic ChipShop, Jena, Germany) were attached using superglue (3M) and sealed using instant-mix epoxy (Loctite, Westlake, OH, USA) to complete a PCB micropump chip. An advantage of the TPLMPT is that the patterns of the microfluidic layer are pre-aligned with the adhesive of the same patterns (**Step 2**), avoiding cumbersome alignment of the patterned microfluidic layer and adhesive. The entire TPLMPT process from a CAD design to a complete chip only took ~ 40 min. Such rapid turn-around time could accelerate the research and development of microfluidic devices.

4 Experimental

4.1 Characterization of the TPLMPT Fabrication Process

We sought to characterize machining precision of the TPLMPT process and compare with that of conventional cut-through laser machining (i.e., not supported by tape liner) [55]. For this comparison, two types of specimens were prepared. For the first sample type, a microfluidic coverslip was constructed using the TPLMPT process. In this characterization, a PCB chip was replaced with a 1-mm-thick transparent PMMA piece for microscope observation (as the PCB obscures light). The second sample type was identical to the first specimen, except that 467MP tapes were attached to the top and bottom of the microfluidic layer *without* the bottom protective tape stack. Not having the tape stack, the tape-PMMA-tape composite sheet was completely penetrated. The difference between the two fabrication methods seems minor but made a significant difference in dimensional accuracy.
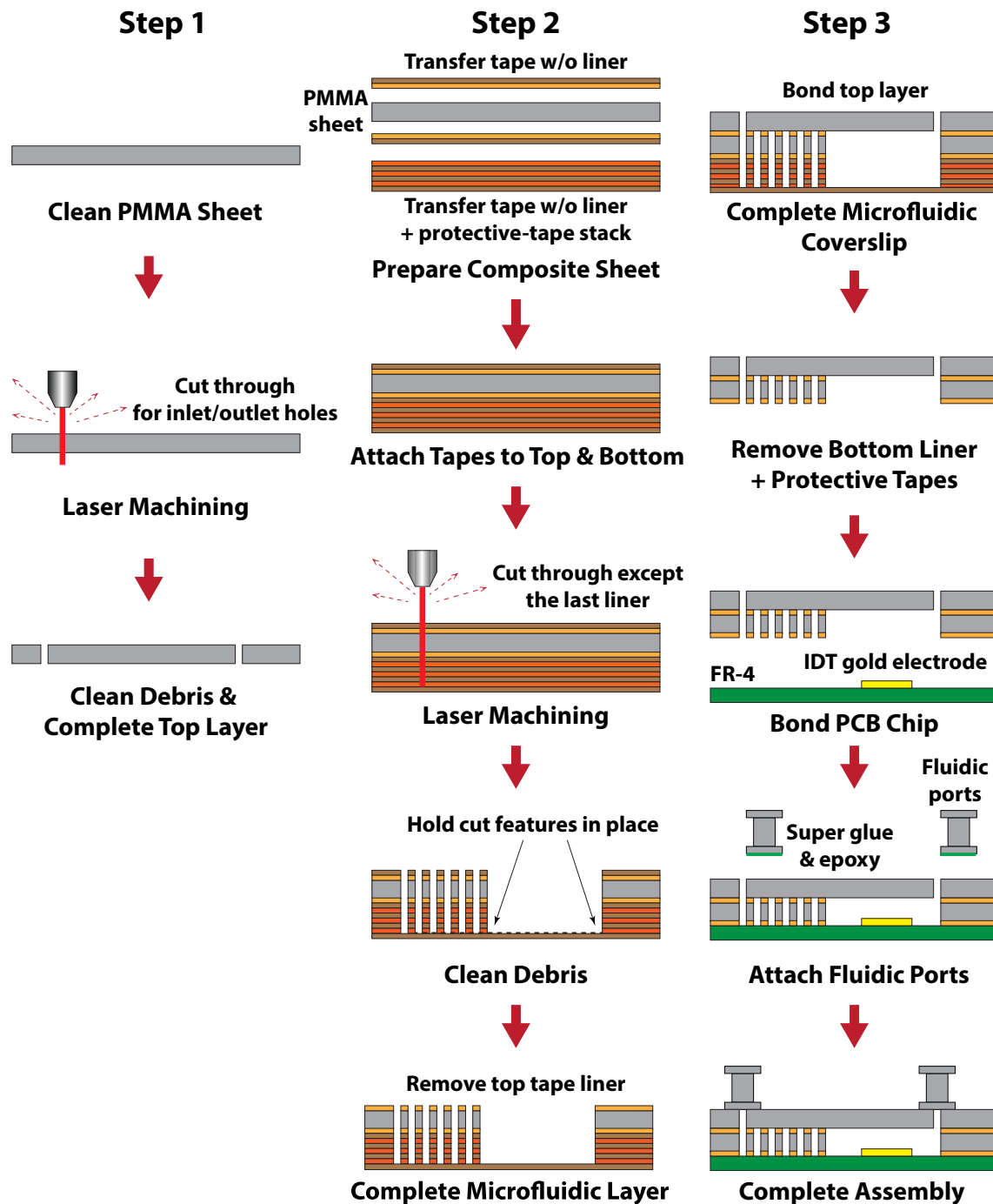
Fig. 3 Tape-liner-supported plastic laser micromachining and pattern transfer (TPLMPT) process. In **Step 1**, the top layer with inlet and outlet holes is prepared with a 1 mm-thick PMMA sheet using laser cutting. In **Step 2**, a tape-PMMA-tape composite layer is prepared by pre-pasting transfer tapes and a stack of protective tapes on a 1-mm-thick PMMA sheet. Using the optimized laser machining, the microfluidic features are cut. However, the last liner of the bottom protective tapes is not penetrated, and the liner holds the machined features in place. In **Step 3**, the top layer (from **Step 2**) is bonded to the microfluidic layer to prepare a microfluidic coverslip after peeling off the top tape liner of the microfluidic layer. The microfluidic coverslip is bonded to a PCB electrode chip after removing the bottom liner of the microfluidic coverslip along with the protective tape stack. The TPLMPT process is finalized by bonding Luer Lok fluidic ports to the microfluidic coverslip using superglue and epoxy

Three samples of each type were scrutinized under the microscope (BX-40) by measuring the width of the serpentine channel (Fig. 2b). The widths at 12 locations along the microchannel (~ 1.5 mm above and below from the tips of the "U" segments and the centers of the vertical channel segments, see Fig. 5b for detail) were measured and averaged. The dimensional accuracy was quantified by RSD (relative standard deviation) of the channel width.

4.2 Electrochemical Activation of Gold Electrodes on a PCB Chip

Fresh gold electrodes on a PCB chip cannot effectively generate flow due to electrochemical inactivity. In electrochemistry, metal electrodes are commonly replenished using surface-treatment techniques such as grinding, polishing, and acid treatment. Then the electrodes are electrochemically "activated" using a train of voltage sweeps and pulses [12, 13, 90]. These methods may remove adsorbed materials through physical or oxidative processes, and induce structural and morphological changes on the electrode surface. The purpose of these methods is to reduce overpotential by enhancing charge transfer between the electrode and electroactive species. In our case, the goal is to improve flow-rate generation by enhancing charge transfer to/from H_2O and H^+ during electrolysis [91]. Since it is challenging to mechanically polish thin PCB gold electrodes, we only relied on electrochemical activation [14, 15]. We compared the pumping performance index (PPI, flow rate generated per given current [8]) of 6 different activation programs using 1 M Na_2SO_4 electrolyte (Sigma). An electrochemical activation program comprising ten sweeps between − 2.15 and 2.25 V at 1 V/s rate and ten pulses between − 1.05 and 1.25 V with an equal duration of 0.5 s was chosen (Fig. S2 in SI). The detailed procedure for the activation is given in Section S3 of SI.

4.3 Measurement of Flow Rate and Backpressure

We custom-built two experimental setups for image-based flow-rate measurement (Fig. 4a), and for simultaneous flow-rate and backpressure measurements (Fig. 4b). These setups are significant upgrades from our previous work [8]. An electrolyte (1 M Na_2SO_4) was loaded into the microfluidic pump using a 1-ml syringe. A dc current (1 mA–2 A) was applied using a precision source meter (B2901A, Keysight Technologies, Santa Rosa, CA, USA). The cell voltage V_{cell} and the power consumption P_{cell} were recorded using the source meter. Gas bubbles generated by electrolysis pressurized the electrolyte, pumping it through the microchannel.

Motion-image-based velocity measurement was used for near-zero backpressure conditions because a downstream flow meter and pressure sensor cause backpressure. The
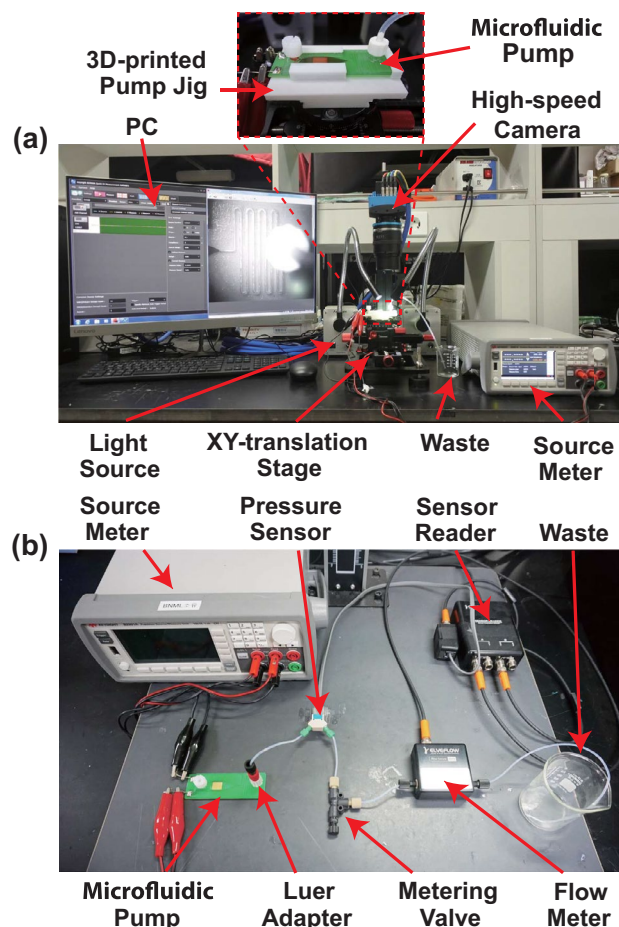

Fig. 4 Experimental setups. **a** Imaging-based flow-rate measurement setup. The source meter supplies dc current to the micropump chip, and concurrently measures power consumption and cell voltage. A high-speed camera equipped with a macro zoom lens is used to capture the motion image of liquid flow inside the microchannel. The micropump is mounted on a custom-built XY-stage. **b** Sensor-based flow-rate and backpressure measurement setup. The pressure sensor and flow meter are used for simultaneously measuring backpressure and flow rate after the metering valve was set for predetermined backpressure. The sensor reader collects and transfers data to a control PC. The PC also controls the source meter

flow motion was recorded using a monochromatic high-speed camera EoSens 4CXP (Mikrotron, Munich, Germany) equipped with a macro zoom lens (MP-E 65 mm f/2.8 1×–5×, Canon, Tokyo, Japan), installed on a custom-built manual XY stage (iShoot, Shenzhen, China) and a camera stand (Wemacro Rail, Shanghai, China). A PC was used to control the camera and store high-speed motion images. Two LED light sources (LED-50W, Amscope, Irvine, CA, USA) were used for illumination. Depending on flow rate, motion image was recorded at 80–8000 frames per second (fps). The motion image was analyzed using ImageJ software (National Institute of Health, Bethesda, MD, USA). The first and third fiducials (Fig. 2b) were captured in the motion picture. The

number of frames between the two fiducials (i.e., time) was used to calculate flow velocity v [mm/s]. The channel height was estimated by measuring the thickness of the microfluidic layer using a Vernier caliper (Mitutoyo, Kawasaki, Japan). Due to variation in the channel cross-sectional area A occurred during chip fabrication, an individual chip was calibrated using a precision syringe pump to accurately calculate flow rate Q [ml/min] from measured flow velocity ($Q = vA$). The procedure for the calibration is detailed in Section S4 of SI.

For backpressure measurement, an in-line flow sensor (MFS-5, Elveflow, Paris, France), pressure sensor (MPS-5, Elveflow), and a micro metering valve (P-446, IDEX Health & Science, Oak Harbor, WA, USA) were used. Both sensors were connected to a sensor reader (MSR, Elveflow), which is linked to the PC for data acquisition. The metering valve was set to a predetermined position for backpressure generation. For a fine adjustment of backpressure (i.e., an orifice size), the knob of the metering valve was divided into 30 sections using a ruler wrapped around the knob. The number of unwinding turns (e.g., 0 turn = fully closed orifice) was recorded for reproducible backpressure experiments (Sect. 5.3). All these components were connected using a 1/16-inch Teflon tube. A limited working volume of the micropump cannot fill all these downstream components including the flow sensor, pressure sensor, and the tubes connecting the sensors. Consequently, these components were filled with electrolyte before pumping so that flow rate and pressure were properly measured. Flow rate and backpressure were simultaneously recorded as a function of time after dc current (0.1–2 A) was applied. The temperature was 23 ± 1 °C.

4.4 Performance Characterization of the Oil Separation Barrier

The oils (Table 1) were examined as a separation barrier in our micropump to assess if (1) an oil plug is stable during pumping, (2) any cross-contamination between electrolyte and working fluid occurs, and (3) oil plug deteriorates pumping performance due to viscosity different from that of water. We selected three low-viscosity oils from Table 1: HFE-7500, hexadecane, and tetradecane. An electrolyte, oil plug, and working fluid were sequentially and carefully loaded into the micropump for stable water–oil-water interfaces. The electrolyte volume was 240 µl, while the total volume of the oil plug and working fluid was 88 µl (tested oil-plug volume: 10, 20, and 30 µl). The detailed procedure for liquid injection is given in Section S5.

After forming stable water–oil-water interfaces, dc currents were applied for pumping, and the stability of moving interfaces was investigated. The current range was 1 mA–2 A, identical to the range in the flow-rate measurement

(Sect. 4.3). After testing the stability, the chip was cleaned, and the liquids were loaded for a next larger current. The stability of moving interfaces was visually examined by the high-speed camera setup (Fig. 4a). Flow rate of concatenated liquid segments was also measured using the same setup. The only difference was the camera; a Nikon 1 J5 (up to 400 fps at 800 × 296 pixels; Tokyo, Japan) equipped with a macro lens (AF-S DX Micro Nikkor 85 mm f/3.5G ED VR) was used for color imaging. In order to distinguish from transparent oil, the electrolyte and working fluid were colored using food-coloring dyes (~0.01 g/ml concentration) in green (Naturals, Gunpo, South Korea) and red (Bowon Food, Anyang, South Korea), respectively.

The stability was characterized by steady separation between the green electrolyte and red working fluid. The largest stable currents and the smallest stable oil volume for each oil were characterized to evaluate stability because the electrolyte-oil or the oil-working fluid interfaces become progressively unstable with an increasing current and decreasing oil volume. First, the smallest plug volume of 10 µL was injected, and the largest current of 2 A was applied. If the interface was stable, then this volume and current were chosen as the stable volume and currents. Otherwise, the current was lowered (e.g., 1.5 A) with the same volume until a stable current was found. If no stable current was found, then the next larger volume of 20 µL was tested with currents in the same decreasing order. This process was repeated until the largest stable current and smallest stable volume (threshold current I_{th} and volume V_{th}) were found for each oil.

In order to study the impact of oils on flow rate, current was applied to the pump with the best oil plug in the largest stable volume, and flow rate was measured in the near-zero backpressure condition (Fig. 4a). A flow rate vs. current curve was constructed to calculate PPI and evaluate the effect.

5 Result

5.1 Characterization of the TPLMPT Process

The tape liner and protective tapes were used to steadily hold the long, narrow, meander microchannel that was cut out of a thin PMMA sheet (Fig. 3). Without this support, the cut PMMA layer was flimsy, and an apparent distortion of microfeatures was observed (Fig. 5). We characterized the machining precision of the TPLMPT process and compared it with that of a conventional cut-through (i.e., trepanning cut [92]) laser machining process.

Microscope images indicate that an average channel width for the three TPLMPT samples was 474 µm (nominal channel width 500 µm), and an average standard deviation was 34.8 µm (RSD = 7.3%) over the three samples.
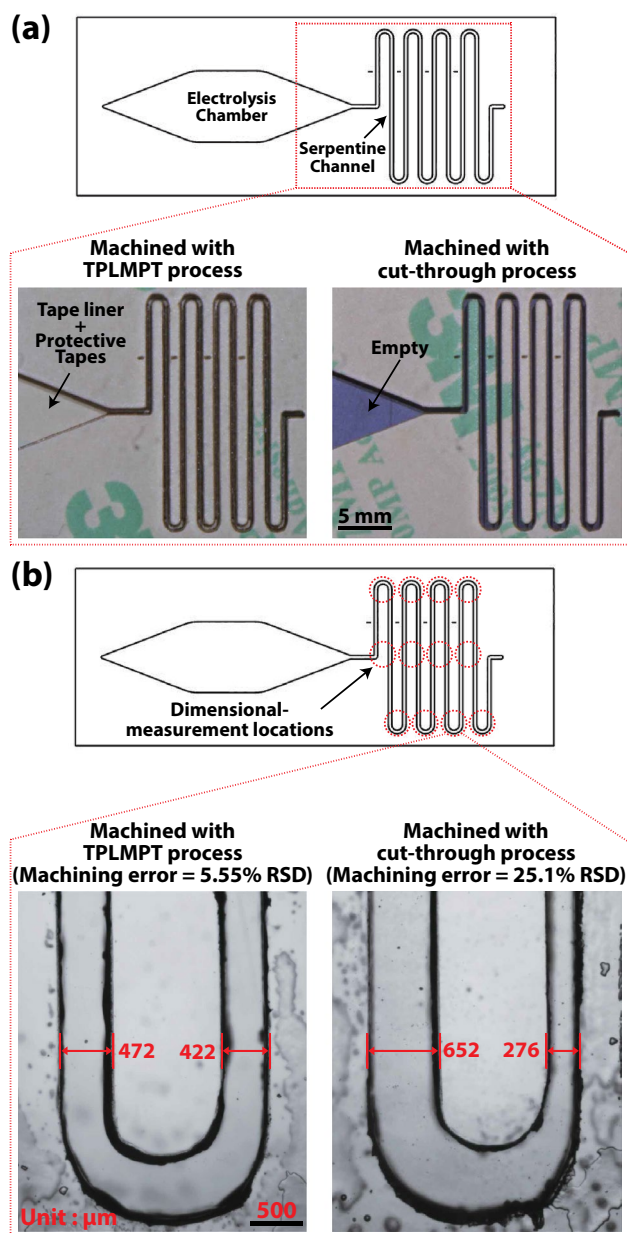
Fig. 5 Comparison of the TPLMPT and cut-through laser cutting. **a** Photographs of the tape-PMMA-tape composite layers after machined with both microfabrication techniques. The distortion of the serpentine channel is apparent in the cut-through sample because the microfeatures are not mechanically supported (i.e., empty) unlike the TPLMPT sample. **b** The 12 locations for channel-width measurement are marked with dotted circles. The relative machining errors over these locations (RSD of 5.55% vs. 25.1%) clearly indicate that the TPLMPT is superior. The micrographs of exemplary "U" channel segments fabricated using both microfabrication techniques are shown with the measured channel widths

Characterization of the cut-through samples yielded an average width of 482 μm and an average standard deviation of 110 μm (RSD = 22.9%). Overall, the TPLMPT process yielded three times more precise machining. For

the best TPLMPT sample (RSD = 5.55% over 12 detection points) and the worst cut-through sample (RSD = 25.1%), the machining precision was almost five times. The magnified photographs of the "U" channel sections (Fig. 5b) clearly demonstrate that the precision of the TPLMPT is superior. We speculate that the poor machining precision of cut-through features may stem from the distortion of the heat-affected zone (HAZ) [93] and unintended movement of infirm microfeatures during bonding. In summary, the designed patterns were transferred to a thin PMMA substrate with a better machining precision using the TPLMPT than the conventional cut-through laser machining.

5.2 Pumping Performance Characterization

Four micropump chips were tested for pumping performance. A variation in the cross-sectional area of the individual chip was calibrated using a precision syringe pump for accurate flow-rate measurement (Section S4 in SI). Figure 6a shows a flow rate vs. current plot of four individual chips for a wide current range of 1 mA–2 A. We observed that flow rate ranged from 5.47 μl/min to 24.49 ml/min under near-zero backpressure conditions. The flow rates for the highest current of 2 A were 22.57–24.49 ml/min, which were similar to 22.64–24.66 ml/min of our previous mesoscale pump [8]. The flow rate was linearly proportional to the current ($R^2 = 0.998$–0.999 for all chips), validating Eq. (1). The PPI (pumping performance index) ranged from 191.7 to 206.7 μl/C, similar to the those of our previous mesoscale pump (196.0–204.0 μl/C) [8]. Consequently, the pumping performance of the new microfluidic pump is similar to that of the mesoscale pump under the near-zero backpressure condition. The current vs. flow rate curve with pooled data (chip #1–4) is shown in Fig. 6b. The PPI variation between chips was only an RSD of 2.353%. The flow rate variation at the highest current 2 A was an RSD of 3.316%. Furthermore, the smallest flow-rate variation was an RSD of 1.765% at 1 A. These results indicate that chip-to-chip performance variation appeared negligible.

The power consumption of pooled chips is shown in Fig. 6c, ranging from 2.77 mW (1 mA) to 11.88 W (2 A). Power consumption was similar to that of our previous pump (2.77–32.5 vs. 2.8–32.9 mW, both measured at 1–10 mA) [8]. The FPP, flow rate per power (the slope of Fig. 6c), was 2.12 ml/min·W. We investigated the FPP of micropumps reported in recent review papers [1–7, 94–103]. The FPP values of 40 published micropumps were lower than ours, typically ranging from 10^{-4} to 10^{-1} ml/min·W. There are 24 cases where the FPP is higher than ours, ranging from 10^1 to 10^5 ml/min·W, but 7 of them required high driving voltages (> 100 V; piezoelectric, electrowetting, electrohydrodynamic, and electrostatic types), 6 of them yielded relatively low flow rate (< 100 μl/min; electrowetting, electroosmotic,
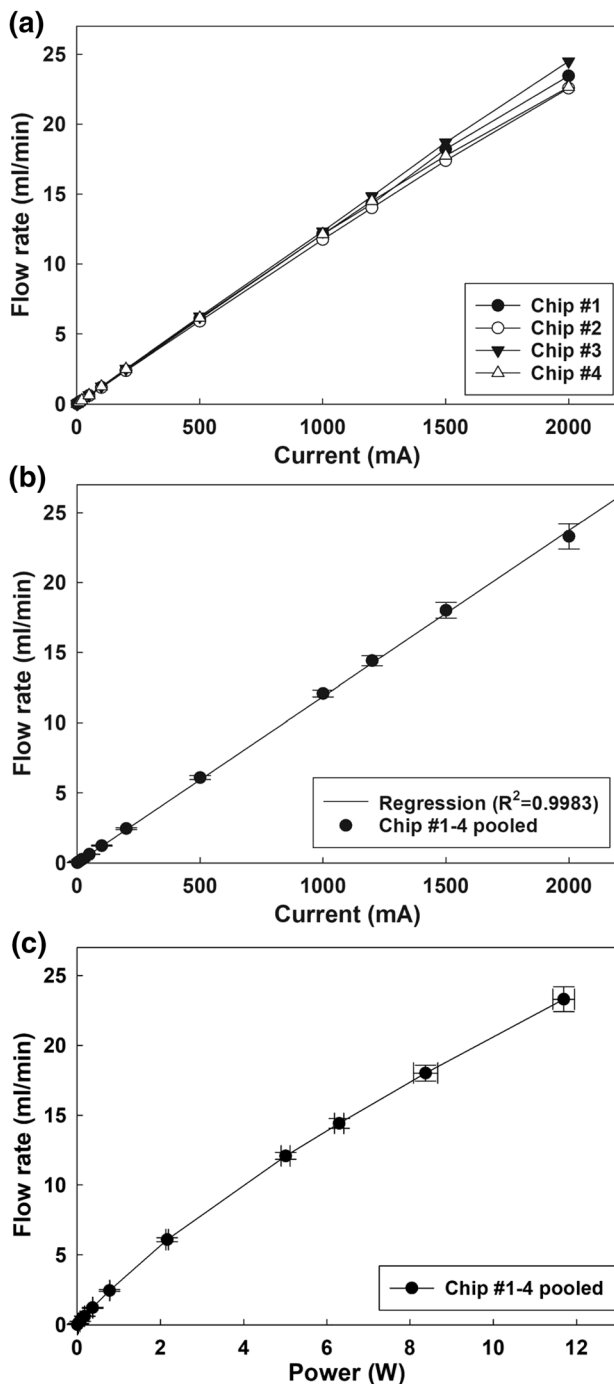
Fig. 6 Flow-rate characterization. **a** Flow rate as a function of dc current. The linearity of curves is $R^2 = 0.999$, 0.999, 0.999, and 0.998 for Chip #1–4, respectively. PPI (pumping performance index), indicating volumetric pumping per consumed electrical charge, ranges from 191.7 to 206.7 μl/C. **b** Flow rate vs. current curve for pooled data. Small PPI variation (RSD = 2.353%) denotes excellent chip-to-chip consistency. **c** Flow rates as a function of power for the pooled chips. Power consumption ranges from 2.77 mW (1 mA) to 11.88 W (2 A)

ferromagnetic, and piezoelectric types), 6 of them needed external components such as a rotating magnet and motor (electromagnetic and rotary types), and the rest of them yield relatively low backpressure (< 60 kPa, see Sect. 5.3 for detail). Furthermore, most of them is manufactured using costly and time-consuming cleanroom-based microfabrication techniques.

5.3 Backpressure Measurement

An excellent flow rate as high as 24.49 ml/min was achieved using our new microfluidic pump. However, flow rate was measured under the near-zero backpressure condition. Backpressure is a critical performance metric, especially for integrated microfluidic devices having a significant head loss owing to a network of long, narrow microchannels. Therefore, the backpressure was measured using the second measurement setup (Fig. 4b).

It is critical to ensure no leakage from the micropump for accurate backpressure measurement. Unlike our previous mesoscale pump that was assembled with screws and nuts, we observed weakened bonding as backpressure increased, characterized by bubble-like features in the tape adhesive (i.e., Saffman-Taylor finger [104]). Eventually, electrolyte leaked out of the chamber with a further increase in backpressure. Therefore, a reasonable bonding condition for backpressure measurement should be defined. Saffman-Taylor fingers are phenomena caused by instability of an interface between two fluids of different viscosity when a less viscous fluid replaces a more viscous one [104]. This fingering instability also occurs in liquid replacing viscoelastic material (e.g., tape adhesives) [105]. We investigated literature on the bonding strength of tape-bonded microfluidic devices. As internal pressure increases, bonding weakens accompanied with growing Saffman-Taylor fingers, and liquid leakage finally occurs. The pressure, at which Saffman-Taylor fingers as well as leakage occurred, was previously defined as the bonding strength in literature [106, 107]. Therefore, we also defined the backpressure in the same manner.

We examined the status of bonding around the electrolysis chamber under a microscope during pumping experiments (Fig. 7). No weakened bonding was observed at backpressure ≤ 280 kPa ("normal regime"). As the backpressure increased (≥ 329 kPa), Saffman-Taylor fingers were formed and started growing at the interface between the microfluidic layer and PCB chip (inset figure *A), but no leakage was observed ("debonding regime"). Lastly, the electrolyte was leaked from the chamber, as backpressure surpassed 463 kPa ("leakage regime"; inset figure *B). These three regimes are overlayed with flow rate vs. backpressure curves for the current of 0.1–2 A. The boundary between the debonding and leakage regimes overlapped,
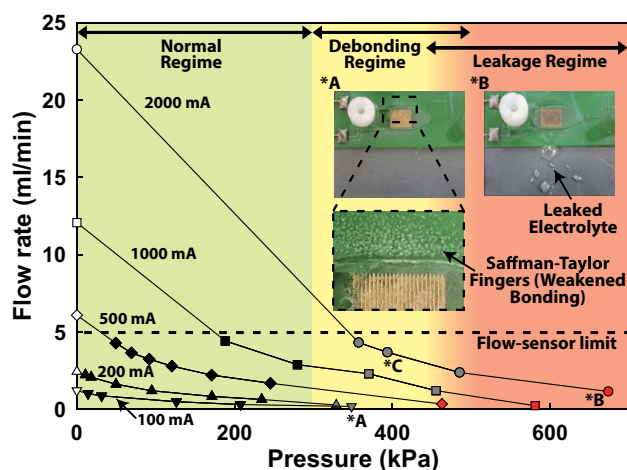
Fig. 7 Backpressure performance. The empty symbols indicate data measured at near-zero backpressure conditions (data from Fig. 6) due to a measurement limit of the flow sensor (i.e., 5 ml/min). The black symbols and "normal regime" indicate the cases where the pump works normally without leakage or sign of delamination. The gray symbols and "debonding regime" represent the cases where the microfluidic layer starts delaminating from the PCB chip. Inset figure *A shows Saffman-Taylor fingers in the PMMA-PCB interface, an indication of weakened bonding (100 mA). The red symbols and "leakage regime" indicate the cases where excessive backpressure causes apparent electrolyte leakage as shown in inset figure *B (2000 mA). *C is the maximum backpressure obtained without leakage

possibly due to manufacturing variation (i.e., variation in bonding strength for each chip). According to this condition, the maximum backpressure was 394 kPa (*C, the largest pressure in the debonding regime before the overlapping area).

As can be seen in Fig. 7, backpressure performance was outstanding considering that the chip was constructed using adhesive tapes: maximum 394 kPa (~3.89 atm) at the flow rate of 3.69 ml/min without leakage. The backpressure was smaller than that of our previous pump assembled using screws and nuts (maximum 547 kPa at 34 µl/min) [8]. However, considering that the size is 42×smaller (5.25 vs. 218 cm^3) and the weight is 46×smaller (7.64 vs. 353 g), the backpressure performance was more than expected. As seen in our previous work, the flow-rate reduction was worsened at higher pressure, considering ideal straight flow rate-backpressure curves. The observed debonding and leakage may have contributed to flow rate reduction at higher pressure, in addition to previously reported causes including gas recombination and diffusion into electrolyte [50]. The data from Fig. 6 were replicated for the 0.5–2 A cases at near zero-backpressure conditions (empty symbols on the ordinate of Fig. 7) because flow rates could not be measured at these currents using the our flow sensor due to measurement limit (i.e., "flow-sensor limit" in Fig. 7) [8].

We compared the backpressure performance of our micropump with those of previous ones presented in recent review papers [1–7, 95–97, 100, 101]. We discovered a total of 16 pumps that claimed better backpressure performance, and 8 of them meet the following criteria: (1) the maximum backpressure was measured, not extrapolated [108]; (2) non-zero flow rate was reported [109], so the flow rate can also be considered for comparison; and (3) "self-contained" micropumps without external moving components such as a motor [110] or roller [111]. The largest group in these pumps was the electroosmotic type that can generate high backpressure of 0.31–20 MPa [112–116]. However, flow rates at these high backpressures were significantly lower (0.001–350 µl/min), and these pumps operated at extremely high driving voltage (0.1–8 kV). Moreover, glass capillary design renders microfluidic integration difficult [112–114, 116]. Furthermore, cleanroom-based fabrication for chip-based electroosmotic pumps requires high costs, long turn-around time, and significant user training [115]. The second largest group belongs to the phase-change micropump generating a backpressure of 5–13 MPa [117–119], but they also required cleanroom-based fabrication. Due to the slow thermal phase change, flow rates were also significantly low (0.75–1.2 µl/min). Except for the micropumps with the aforementioned disadvantages, our micropump yielded the best backpressure performance. Furthermore, our pump is manufactured using the cleanroom-free TPLMPT process and requires generous driving voltage (i.e., maximum 6 V).

Taken together with the FPP analysis (Sect. 5.2), our electrolytic micropump is an overall excellent microscale pressure source with balanced flow rate, backpressure, power consumption, form factor, and manufacturability.

5.4 Performance of Oil Separation Barrier

We compared the stability of a separation barrier made with each of the three selected oils (i.e., HFE-7500, hexadecane, tetradecane) with varying oil volumes (10, 20, and 30 µl) and currents (1, 2, 5, 10, 20, 50, 100, 200, 500, 100, 1200, 1500, and 2000 mA). Increasing oil volumes (i.e., longer plug) may improve the interfacial stability but can reduce flow rate due to their higher viscosities than that of water (especially hexadecane and tetradecane).

Table 2 summarizes the results of this stability test obtained by visual observation (i.e., intermixing between the red-colored electrolyte and the green-colored working fluid). The electrolyte co-flew with the HEF-7500 oil plug without breaking the interface up to 2000 mA. However, migrating plugs penetrated through the interface between the oil and working fluid toward the channel sidewall, leaving residual working fluid droplets. These droplets were subsequently merged with the trailing electrolyte, although the reverse did not happen to the working fluid (i.e., not

Table 2 Stability test of separation barrier with different oil types and volumes

Oil type	HEF-7500			Tetradecane			Hexadecane		
Oil volume (µl)	10	20	30	10	20	30	10	20	30
Maximum allowable current I_{th} (mA) without contamination	200	200	200	$–^a$	–	–	–	–	–

^{a}Not available

Fig. 8 Stability test of oil separation barriers. The figure on the top denotes the imaging area during pumping. Bubbles formed on the IDT denotes electrolysis reaction. **a** HFE-7500 oil plug. The electrolyte (green) was contaminated by residual working-fluid droplets (red) left while flowing with an oil volume of 10 µL and a current of 1000 mA (the upper panel). Interfaces of electrolyte-oil and oil-working fluid were stable, and no evidence of intersegmental contamination was observed with the same oil volume and a current of 200 mA (the lower panel). **b** Tetradecane oil plug. Both interfaces were unstable even at a mild condition of 10 mA when the oil volume is 10 µL, resulting in intersegmental contamination (the upper panel). Electrolyte contamination (no working-fluid contamination) was observed at a larger oil volume of 30 µL at 1 mA (the lower panel). However, stable interfaces were not observed any of tested conditions. **c** Hexadecane oil plug. A similar trend was observed: intersegmental contamination with 10 µL and 10 mA (the upper panel) and electrolyte contamination with 20 µL and 1 mA (the lower panel). No stable interfaces were observed for any tested conditions
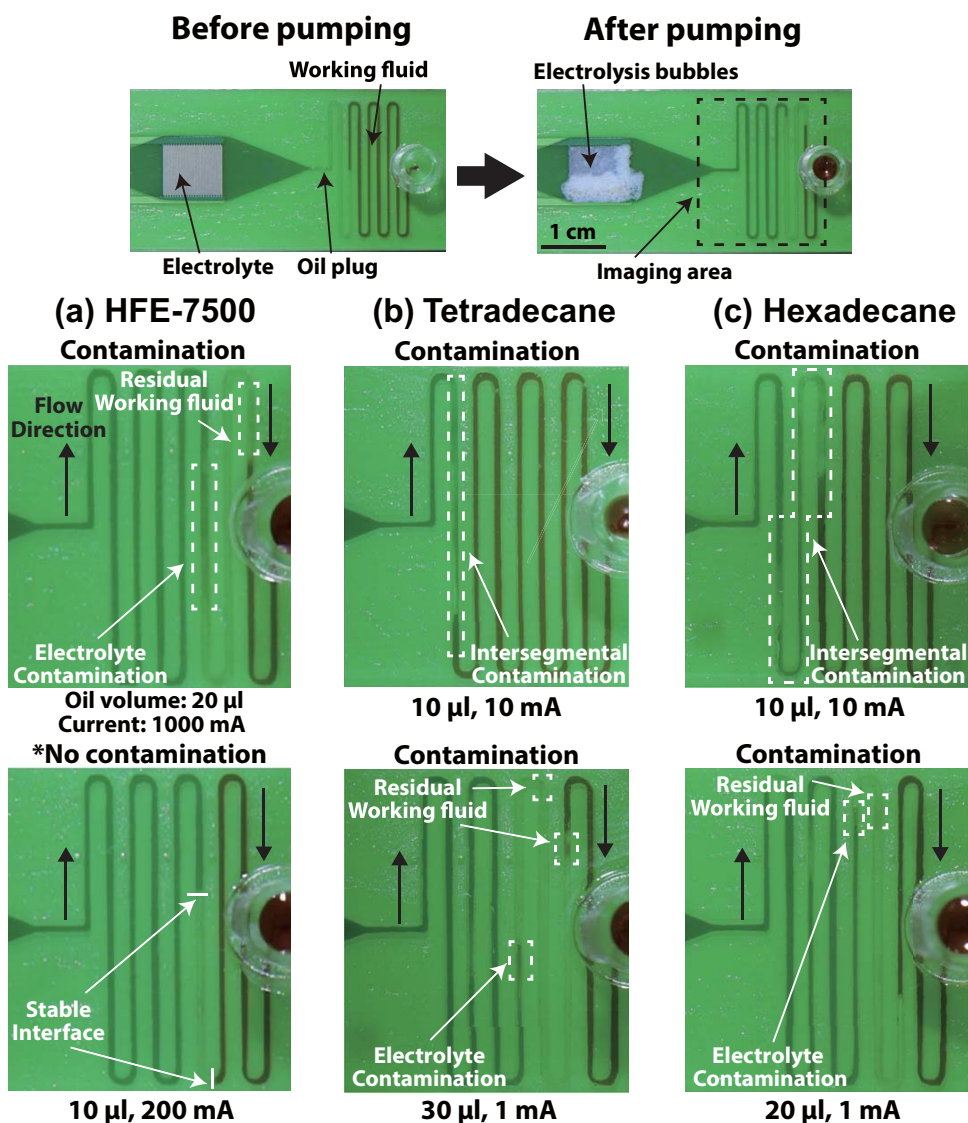
mixed with the trailing electrolyte). The result for 1000 mA current and 10 µl oil volume shows residual working fluid (dim red color) and contaminated electrolyte (green mixed with red) in Fig. 8a (the upper panel). In this condition, the working fluid was not contaminated by the electrolyte, but a small portion of the working fluid was lost during pumping. As the electrolyte is a part of the pump, this condition may be acceptable for certain applications where the loss of sample or reagent (i.e., working fluid) is not critical. Both electrolyte-oil and oil-working fluid interfaces were stable for the currents equal and lower than 200 mA as in Fig. 8a (the lower panel). So the threshold current I_{th} was 200 mA for the 10 µl oil volume as in Table 2. In this condition, neither electrolyte nor working fluid was contaminated or lost, indicating the micropump worked as intended. An increasing volume of the oil plug did not improve the interfacial stability (i.e., electrolyte contamination at currents larger than 200 mA with the 20 and 30 µL oil volumes; Table 2).

Thus, the threshold oil volume V_{th} was 10 μL. In summary, $I_{th} = 200$ mA at $V_{th} = 10$ μL was determined as the stable working condition for HFE-7500.

For the tetradecane, stable interfaces could not be observed for any currents and volumes. We observed consistent intersegmental contamination for any currents with the 10 μl oil volume (working fluid intermixed with electrolyte over the oil plug; the upper panel of Fig. 8b). The result was improved at higher oil volumes; instead of intersegmental contamination, electrolyte contamination by residual working-fluid droplets, in other word no working-fluid contamination, was observed for all tested currents with the 20 μL and 30 μl oil volumes (Fig. 8b, the lower panel). The result is slightly better for the hexadecane. A similar intersegmental contamination occurred for the 10 mA current with the 10 μl oil volume (Fig. 8c, the upper panel). However, electrolyte contamination was observed for the currents lower than 10 mA with this oil volume and for all currents with the 20 μl and 30 μl volumes (Fig. 8c, the lower panels). We speculate that the electrolyte slid under the oil plugs compromising the interfaces and eventually was mixed with the working fluid as the density of water is higher than those of tetradecane and hexadecane unlike HFE-7500 (Table 1). Taken together, the HFE-7500 was chosen for the oil plug material due to the best stability. The maximum allowable current I_{th} and the minimum oil-plug volume V_{th} were again determined as 200 mA and 10 μl, respectively.

Next, we examined if the HFE-7500 plug influences the flow rate. An oil volume of 30 μl was chosen to maximize the influence on the flow rate. Currents of 1, 10, 100, and 200 mA were applied as I_{th} is 200 mA. As seen in Fig. 9,
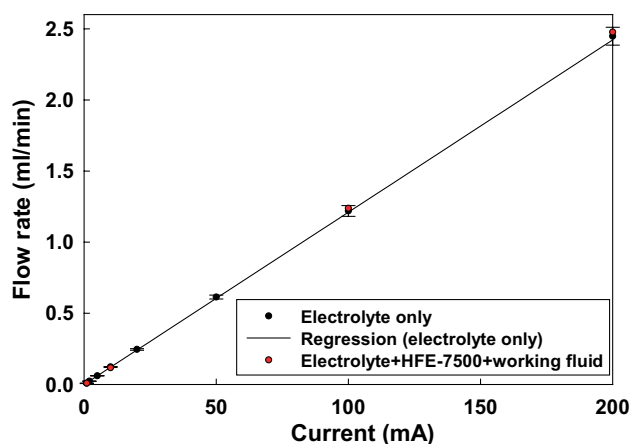

Fig. 9 Flow rate vs. current data for the HFE-7500 oil plug overlaid with the control case (electrolyte-only pumping from Fig. 6b). The volumes of oil plug and working fluid were 30 and 58 μl, respectively. The PPI (pumping-performance index) of the HFE-7500 case was 206.3 μl/C, falling within the variation of the PPI for the control case (198.0–209.7 μl/C), indicating that the oil plug did not deteriorate the pumping performance

the data (red circles) were overlaid with the current vs. flow rate curve of the electrolyte-only pumping experiment (from Fig. 6b). The PPI for the HFE-7500 plug was 206.3 μL/C, falling within the PPI variation of electrolyte-only pumping (i.e., 198.0–209.7 μL/C); all data points for the oil plug lie within the standard deviation of electrolyte-only pumping case for each current. Therefore, we concluded that the impact of the oil plug on flow rates was negligible. We speculate that the effective viscosity of concatenated liquids flowing inside the channel can be similar to the electrolyte viscosity because the viscosity of HFE-7500 is 86% of the water viscosity (Table 1) and the length of oil plug is only ~ 34% of that of the entire liquid filling the microchannel. Consequently, we determined HEF-7500 as the best plug oil because of (1) excellent interfacial stability, (2) minimal impact on pumping performance, (3) high vapor pressure (less evaporation), and (4) inflammability.

6 Conclusion

Our previous PCB-based electrolytic pump demonstrated excellent pumping performance including exceptional backpressure and flow rate [8]. Compared to the pump with the photolithographically fabricated chip, one with the PCB exhibited lower power consumption, longer lifetime, and yet a similar flow rate at a lower manufacturing cost. Moreover, the PCB manufacturing processes yielded machining accuracy adequate for a microfluidic device.

As an on-going endeavor for miniaturization and performance advances from the previous device, we resorted to a simple yet precise tape-based laser-machining process dubbed TPLMPT. The machining precision was improved compared to conventional cut-through laser machining. The TPLMPT displayed three times better machining precision because the appended protective tape stack and liners mechanically held delicate microfluidic features in place during bonding. In addition, the bonding process does not require dedicated instruments (thermal bonding) or toxic chemicals (solvent-assisted bonding). Using the TPLMPT, a fully functional micropump was manufactured from a CAD design in only ~ 40 min so that that design can be rapidly iterated for device development. Such facile design iteration is difficult to achieve in soft lithography (PDMS) or other thermoplastic microfabrication methods (e.g., injection molding or hot embossing) where master mold fabrication is slow and costly.

We demonstrated a "true" microfluidic pump with an excellent pumping performance of a maximum flow rate of 24.49 ml/min and a maximum backpressure of 394 kPa (~3.89 atm; at a flow rate of 3.69 ml/min). Such high pumping performance was aided by an in-house developed electrochemical activation scheme. The backpressure performance was

not as good as our previous micropump that was assembled using screws and nuts (maximum backpressure of 547 kPa at 34 µl/min). Nevertheless, considering 42× smaller size and 46× lighter weight, the backpressure was outstanding. This backpressure performance may also be sufficient for many of microfluidic devices with a relatively simple microchannel network. Moreover, considering a PPI of ~200 µl/C and an FPP of ~2 ml/min·W, our electrolytic micropump is deemed as an effective and energy-efficient pressure source.

In order to overcome the inherent performance limitations of previous electrolytic micropumps due to anchored diaphragm-based separation barriers, we opted for novel, untethered oil plugs. Separation plugs made of fluorinated oil (HFE-7500) and paraffin hydrocarbon oils (tetradecane and hexadecane) were tested for interfacial stability and impacts on flow rate. Tetradecane and hexadecane were unstable (i.e., intersegmental mixing) for examined currents and oil volumes. However, the HFE-7500 was stable up to 200 mA for all tested plug volumes (10 – 30 µl). Therefore, HFE-7500 was chosen as the barrier liquid.

We are currently working on analyzing the long-term stability of the oil separation barrier in various storage conditions of the micropump. In addition, a long-term impact of oil on the chip integrity (i.e., bonding) is underway. We believe our novel PCB electrolytic micropump with the oil separation barrier will expand its applicability to various LOC devices in the future because of its notable performance, easy fabrication, low operating voltage, low power consumption, and relatively straightforward integration with LOCs.

Declarations

Conflict of interest The authors declare that they have no conflict of interest.

References

1. Nisar, A., Afzulpurkar, N., Mahaisavariya, B., Tuantranont, A.: MEMS-based micropumps in drug delivery and biomedical applications. Sens. Actuators B Chem. **130**, 917–942 (2008)
2. Wang, X., Cheng, C., Wang, S., Liu, S.: Electroosmotic pumps and their applications in microfluidic systems. Microfluid. Nanofluid. **6**, 145–162 (2009)
3. Forouzandeh, F., Arevalo, A., Alfadhel, A., Borkholder, D.A.: A review of peristaltic micropumps. Sens. Actuators A Phys. **326**, 112602 (2021)
4. Mohith, S., Karanth, P.N., Kulkarni, S.: Recent trends in mechanical micropumps and their applications: a review. Mechatronics **60**, 34–55 (2019)
5. Wang, Y.-N., Fu, L.-M.: Micropumps and biomedical applications—a review. Microelectron. Eng. **195**, 121–138 (2018)
6. Bußmann, A.B., Grünerbel, L.M., Durasiewicz, C.P., Thalhofer, T.A., Wille, A., Richter, M.: Microdosing for drug delivery application—a review. Sens. Actuators A Phys. **330**, 112820 (2021)
7. Laser, D.J., Santiago, J.G.: A review of micropumps. J. Micromech. Microeng. **14**, R35 (2004)
8. Kim, H., Hwang, H., Baek, S., Kim, D.: Design, fabrication and performance evaluation of a printed-circuit-board microfluidic electrolytic pump for lab-on-a-chip devices. Sens. Actuators A Phys. **277**, 73–84 (2018)
9. Cameron, C.G., Freund, M.S.: Electrolytic actuators: alternative, high-performance, material-based devices. Proc. Natl. Acad. Sci. USA **99**, 7827–7831 (2002)
10. Neagu, C.R., Gardeniers, J.G., Elwenspoek, M., Kelly, J.J.: An electrochemical microactuator: principle and first results. J. Microelectromech. Syst. **5**, 2–9 (1996)
11. O'Keefe, D., O'herlihy, C., Gross, Y., Kelly, J.: Patient-controlled analgesia using a miniature electrochemically driven infusion pump. Br. J. Anaesth. **73**, 843–846 (1994)
12. Hanssen, B.L., Siraj, S., Wong, D.K.: Recent strategies to minimise fouling in electrochemical detection systems. Rev. Anal. Chem **35**, 1–28 (2016)
13. McGlynn, J.C., Friskey, M., Ganin, A.Y.: Parameter optimisation for electrochemically activated MoTe 2. Sustain. Energy Fuels **4**, 4473–4477 (2020)
14. Kim, D., Goldberg, I.B., Judy, J.W.: Microfabricated electrochemical nitrate sensor using double-potential-step chronocoulometry. Sens. Actuators B Chem. **135**, 618–624 (2009)
15. Kim, D., Goldberg, I.B., Judy, J.W.: Chronocoulometric determination of nitrate on silver electrode and sodium hydroxide electrolyte. Analyst **132**, 350–357 (2007)
16. Shamkhalichenar, H., Bueche, C.J., Choi, J.-W.: Printed Circuit Board (PCB) technology for electrochemical sensors and sensing platforms. Biosensors **10**, 159 (2020)
17. Zhao, W., Tian, S., Huang, L., Liu, K., Dong, L.: The review of Lab-on-PCB for biomedical application. Electrophoresis **41**, 1433–1445 (2020)
18. Fu, Y., Yuan, Q., Guo, J.: Lab-on-PCB-based micro-cytometer for circulating tumor cells detection and enumeration. Microfluid. Nanofluid. **21**, 20 (2017)
19. Moschou, D., Tserepi, A.: The lab-on-PCB approach: tackling the µTAS commercial upscaling bottleneck. Lab Chip **17**, 1388–1405 (2017)
20. Richter, S., Nguyen, N.-T., Wego, A., Pagel, L.: Microfluidic devices on printed circuit board. In: Tay, F.E.H. (ed.) Microfluidics and BioMEMS Applications, pp. 185–217. Springer, New York (2002)
21. Wego, A., Richter, S., Pagel, L.: Fluidic microsystems based on printed circuit board technology. J. Micromech. Microeng. **11**, 528–531 (2001)
22. Chang, Y., You, H.: Efficient bond of PDMS and printed circuit board with an application on continuous-flow polymerase chain reaction. Biochip J. **14**, 349–357 (2020)
23. Hassibi, A., Manickam, A., Singh, R., Bolouki, S., Sinha, R., Jirage, K.B., McDermott, M.W., Hassibi, B., Vikalo, H., Mazarei, G., Pei, L., Bousse, L., Miller, M., Heshami, M., Savage,

M.P., Taylor, M.T., Gamini, N., Wood, N., Mantina, P., Grogan, P., Kuimelis, P., Savalia, P., Conradson, S., Li, Y., Meyer, R.B., Ku, E., Ebert, J., Pinsky, B.A., Dolganov, G., Van, T., Johnson, K.A., Naraghi-Arani, P., Kuimelis, R.G., Schoolnik, G.: Multiplexed identification, quantification and genotyping of infectious agents using a semiconductor biochip. Nat. Biotechnol. **36**, 738 (2018)

24. Kricka, L.J., Fortina, P., Panaro, N.J., Wilding, P., Alonso-Amigo, G., Becker, H.: Fabrication of plastic microchips by hot embossing. Lab Chip **2**, 1–4 (2002)

25. Ladner, Y., Liu, D., Montels, J., Morel, J., Perrin, C.: Enzymatic reaction automation in nanodroplet microfluidic for the quality control of monoclonal antibodies. Biochip J. **16**, 317–325 (2022)

26. Giboz, J., Copponnex, T., Mélé, P.: Microinjection molding of thermoplastic polymers: a review. J. Micromech. Microeng. **17**, R96 (2007)

27. Jo, D., Kim, S.Y., Kang, H.W., Pyo, S.H., Jeong, N.K., Bae, N.H., Lee, S.J., Kim, Y.T., Lee, K.G.: Micro-injection molded droplet generation system for digital PCR application. Biochip J. **16**, 433–440 (2022)

28. McDonald, J.C., Duffy, D.C., Anderson, J.R., Chiu, D.T., Wu, H., Schueller, O.J., Whitesides, G.M.: Fabrication of microfluidic systems in poly (dimethylsiloxane). Electrophoresis **21**, 27–40 (2000)

29. Klank, H., Kutter, J.P., Geschke, O.: CO 2-laser micromachining and back-end processing for rapid production of PMMA-based microfluidic systems. Lab Chip **2**, 242–246 (2002)

30. Han, H., Choi, S.-J.: Development of an inkless, visual volumetric chip operated with a micropipette. Biochip J. **15**, 179–186 (2021)

31. Guckenberger, D.J., de Groot, T.E., Wan, A.M., Beebe, D.J., Young, E.W.: Micromilling: a method for ultra-rapid prototyping of plastic microfluidic devices. Lab Chip **15**, 2364–2378 (2015)

32. Lee, S., Kim, J.H., Kang, S.J., Chang, I.H., Park, J.Y.: Customized multilayered tissue-on-a-chip (MToC) to simulate bacillus Calmette-Guérin (BCG) immunotherapy for bladder cancer treatment. Biochip J. **16**, 67–81 (2022)

33. Bartholomeusz, D.A., Boutté, R.W., Andrade, J.D.: Xurography: rapid prototyping of microstructures using a cutting plotter. J. Microelectromech. Syst. **14**, 1364–1374 (2005)

34. Bhattacharjee, N., Urrios, A., Kang, S., Folch, A.: The upcoming 3D-printing revolution in microfluidics. Lab Chip **16**, 1720–1742 (2016)

35. Namgung, H., Kaba, A.M., Oh, H., Jeon, H., Yoon, J., Lee, H., Kim, D.: Quantitative determination of 3D-printing and surface-treatment conditions for direct-printed microfluidic devices. Biochip J. **16**, 82–98 (2022)

36. Aladese, A.D., Jeong, H.-H.: Recent developments in 3D printing of droplet-based microfluidics. Biochip J. **15**, 313–333 (2021)

37. Abgrall, P., Conedera, V., Camon, H., Gue, A.-M., Nguyen, N.-T.: SU-8 as a structural material for labs-on-chips and microelectromechanical systems. Electrophoresis **28**, 4539–4551 (2007)

38. Webster, J., Burns, M., Burke, D., Mastrangelo, C.: Monolithic capillary electrophoresis device with integrated fluorescence detector. Anal. Chem. **73**, 1622–1626 (2001)

39. Becker, H., Locascio, L.E.: Polymer microfluidic devices. Talanta **56**, 267–287 (2002)

40. Soper, S.A., Ford, S.M., Qi, S., McCarley, R.L., Kelly, K., Murphy, M.C.: Polymeric microelectromechanical systems. Anal. Chem. **72**, 642A-651A (2000)

41. Wang, Z., Zheng, H., Lim, R., Wang, Z., Lam, Y.: Improving surface smoothness of laser-fabricated microchannels for microfluidic application. J. Micromech. Microeng. **21**, 095008 (2011)

42. Yuan, D., Das, S.: Experimental and theoretical analysis of direct-write laser micromachining of polymethyl methacrylate by CO 2 laser ablation. J. Appl. Phys. **101**, 024901 (2007)

43. Khan Malek, C.G.: Laser processing for bio-microfluidics applications (part I). Anal. Bioanal. Chem. **385**, 1351–1361 (2006)

44. Nath, P., Fung, D., Kunde, Y.A., Zeytun, A., Branch, B., Goddard, G.: Rapid prototyping of robust and versatile microfluidic components using adhesive transfer tapes. Lab Chip **10**, 2286–2291 (2010)

45. Mohammed, M., Abraham, E., Desmulliez, M.: Rapid laser prototyping of valves for microfluidic autonomous systems. J. Micromech. Microeng. **23**, 035034 (2013)

46. Macdonald, N.P., Cabot, J.M., Smejkal, P., Guijt, R.M., Paull, B., Breadmore, M.C.: Comparing microfluidic performance of three-dimensional (3D) printing platforms. Anal. Chem. **89**, 3858–3866 (2017)

47. Au, A.K., Lee, W., Folch, A.: Mail-order microfluidics: evaluation of stereolithography for the production of microfluidic devices. Lab Chip **14**, 1294–1301 (2014)

48. Prakash, S., Kumar, S.: Fabrication of microchannels on transparent PMMA using CO 2 Laser (10.6 μm) for microfluidic applications: an experimental investigation. Int. J. Precis. Eng. Manuf. **16**, 361–366 (2015)

49. Hoople, G.D., Rolfe, D.A., McKinstry, K.C., Noble, J.R., Dornfeld, D.A., Pisano, A.P.: Comparison of microscale rapid prototyping techniques. J. Micro. Nanomanuf. **2**, 034502-034502–034506 (2014)

50. Tsao, C.-W., DeVoe, D.L.: Bonding of thermoplastic polymer microfluidics. Microfluid. Nanofluid. **6**, 1–16 (2009)

51. Liga, A., Morton, J.A., Kersaudy-Kerhoas, M.: Safe and cost-effective rapid-prototyping of multilayer PMMA microfluidic devices. Microfluid. Nanofluid. **20**, 164 (2016)

52. Jung, B.-J., Jang, H., Lee, G.-Y., Kim, J., Song, Z., Pyun, J.-C., Lee, W.: Surface functionalization and bonding of chemically inert parylene microfluidics using parylene—a adhesive layer. Biochip J. **16**, 168–174 (2022)

53. Liu, H., Crooks, R.M.: Three-dimensional paper microfluidic devices assembled using the principles of origami. J. Am. Chem. Soc. **133**, 17564–17566 (2011)

54. Patko, D., Mártonfalvi, Z., Kovacs, B., Vonderviszt, F., Kellermayer, M., Horvath, R.: Microfluidic channels laser-cut in thin double-sided tapes: cost-effective biocompatible fluidics in minutes from design to final integration with optical biochips. Sens. Actuators B Chem. **196**, 352–356 (2014)

55. Kim, J., Shin, Y., Song, S., Lee, J., Kim, J.: Rapid prototyping of multifunctional microfluidic cartridges for electrochemical biosensing platforms. Sens. Actuators B Chem. **202**, 60–66 (2014)

56. Furdui, V.I., Kariuki, J.K., Harrison, D.J.: Microfabricated electrolysis pump system for isolating rare cells in blood. J. Micromech. Microeng. **13**, S164–S170 (2003)

57. Böhm, S., Olthuis, W., Bergveld, P.: An integrated micromachined electrochemical pump and dosing system. Biomed. Microdev. **1**, 121–130 (1999)

58. Böhm, S., Timmer, B., Olthuis, W., Bergveld, P.: A closed-loop controlled electrochemically actuated micro-dosing system. J. Micromech. Microeng. **10**, 498–504 (2000)

59. Lee, S.W., Sim, W.Y., Yang, S.S.: Fabrication and in vitro test of a microsyringe. Sens. Actuators A Phys. **83**, 17–23 (2000)

60. Kabata, A., Okamura, K., Suzuki, H., Kishigami, Y., Kikuchi, M., Haga, M.: Prototype micropump for insulin administration based on electrochemical bubble formation. J. Pharm. Sci. **97**, 5037–5045 (2008)

61. Yi, Y., Zaher, A., Yassine, O., Kosel, J., Foulds, I.G.: A remotely operated drug delivery system with an electrolytic pump and a thermo-responsive valve. Biomicrofluidics **9**, 052608 (2015)

62. Metref, L., Herrera, F., Berdat, D., Gijs, M.A.: Contactless electrochemical actuator for microfluidic dosing. J. Microelectromech. Syst. **16**, 885–892 (2007)

63. Lui, C., Stelick, S., Cady, N., Batt, C.: Low-power microfluidic electro-hydraulic pump (EHP). Lab Chip **10**, 74–79 (2010)

64. Sheybani, R., Meng, E.: Acceleration techniques for recombination of gases in electrolysis microactuators with Nafion®-coated electrocatalyst. Sens. Actuators B Chem. **221**, 914–922 (2015)

65. Li, P.-Y., Sheybani, R., Gutierrez, C.A., Kuo, J.T., Meng, E.: A parylene bellows electrochemical actuator. J. Microelectromech. Syst. **19**, 215–228 (2010)

66. Portilla, J.M., Kim, U.: In: IEEE 26th International Conference on Micro Electro Mechanical Systems, pp. 1077–1080. IEEE, Taipei (2013)

67. Munyan, J.W., Fuentes, H.V., Draper, M., Kelly, R.T., Woolley, A.T.: Electrically actuated, pressure-driven microfluidic pumps. Lab Chip **3**, 217–220 (2003)

68. Chiu, S.-H., Liu, C.-H.: An air-bubble-actuated micropump for on-chip blood transportation. Lab Chip **9**, 1524–1533 (2009)

69. Xie, J. California Institute of Technology (2005)

70. Liu, R.H., Nguyen, T., Schwarzkopf, K., Fuji, H.S., Petrova, A., Siuda, T., Peyvan, K., Bizak, M., Danley, D., McShea, A.: Fully integrated miniature device for automated gene expression DNA microarray processing. Anal. Chem. **78**, 1980–1986 (2006)

71. Olthuis, W., Streekstra, W., Bergveld, P.: Theoretical and experimental determination of cell constants of planar-interdigitated electrolyte conductivity sensors. Sens. Actuators B Chem. **24**, 252–256 (1995)

72. Atencia, J., Beebe, D.J.: Controlled microfluidic interfaces. Nature **437**, 648 (2004)

73. Teh, S.-Y., Lin, R., Hung, L.-H., Lee, A.P.: Droplet microfluidics. Lab Chip **8**, 198–220 (2008)

74. Zheng, B., Tice, J.D., Roach, L.S., Ismagilov, R.F.: A droplet-based, composite PDMS/Glass capillary microfluidic system for evaluating protein crystallization conditions by microbatch and vapor-diffusion methods with on-chip X-ray diffraction. Angew. Chem. Int. Ed. **43**, 2508–2511 (2004)

75. Shum, H.C., Kim, J.-W., Weitz, D.A.: Microfluidic fabrication of monodisperse biocompatible and biodegradable polymersomes with controlled permeability. J. Am. Chem. Soc. **130**, 9543–9549 (2008)

76. http://multimedia.3m.com/mws/media/247250O/thermal-management-fluids-and-services-brochure.pdf. Accessed 11 Jan 2023

77. http://www.ddbst.com/en/EED/PCP/VIS_C516.php. Accessed 11 Jan 2023

78. https://pubchem.ncbi.nlm.nih.gov/compound/11006. Accessed 11 Jan 2023

79. https://www.arb.ca.gov/db/solvents/solvent_pages/Hydrocarbon-HTML/Mineral_Oil.htm. Accessed 11 Jan 2023

80. https://pubchem.ncbi.nlm.nih.gov/compound/Tetradecane. Accessed 11 Jan 2023

81. https://www.sigmaaldrich.com/MSDS/retriever.do?country=IE&language=EN&productNumber=330779&brand=SIAL. Accessed 11 Jan 2023

82. https://www.acrylite.net/product/acrylite/downloads/1554c-chemical-resistance-chart.pdf. Accessed 24 Oct 2018

83. https://pubchem.ncbi.nlm.nih.gov/compound/962#section=Top. Accessed 11 Jan 2023

84. http://www.wiredchemist.com/chemistry/data/vapor-pressure. Accessed 11 Jan 2023

85. Lu, L., Hou, D., Fang, Y., Huang, Y., Ren, Z.J.: Nickel based catalysts for highly efficient H2 evolution from wastewater in microbial electrolysis cells. Electrochim. Acta **206**, 381–387 (2016)

86. Liu, S., Lei, Y.-J., Xin, Z.-J., Lu, Y.-B., Wang, H.-Y.: Water splitting based on homogeneous copper molecular catalysts. J. Photochem. Photobiol. A: Chem. **355**, 141–151 (2018)

87. Kaba, A.M., Jeon, H., Park, A., Yi, K., Baek, S., Park, A., Kim, D.: Cavitation-microstreaming-based lysis and DNA extraction using a laser-machined polycarbonate microfluidic chip. Sens. Actuators B Chem. **346**, 130511 (2021)

88. Giri, K., Tsao, C.-W.: Recent advances in thermoplastic microfluidic bonding. Micromachines **13**, 486 (2022)

89. https://www.pstc.org/files/public/Theisen_John.pdf. Accessed 11 Jan 2023

90. Wang, J., Pedrero, M., Sakslund, H., Hammerich, O., Pingarron, J.: Electrochemical activation of screen-printed carbon strips. Analyst **121**, 345–350 (1996)

91. Wang, J., Hutchins, L.D.: Activation of glassy carbon electrodes by alternating current electrochemical treatment. Anal. Chim. Acta **167**, 325–334 (1985)

92. Choudhury, I., Chong, W., Vahid, G.: Hole qualities in laser trepanning of polymeric materials. Opt. Lasers Eng. **50**, 1297–1305 (2012)

93. Miraoui, I., Boujelbene, M. Zaied, M.: High-power laser cutting of steel plates: heat affected zone analysis. Adv. Mater. Sci. Eng. **2016** (2016)

94. Yun, K.-S., Yoon, E.: Micropumps for MEMS/NEMS and microfluidic systems. In: Leondes, C.T. (ed.) MEMS/NEMS Handbook Techniques and Applications, pp. 1112–1144. Springer, New York (2006)

95. Amirouche, F., Zhou, Y., Johnson, T.: Current micropump technologies and their biomedical applications. Microsyst. Technol. **15**, 647–666 (2009)

96. Iverson, B.D., Garimella, S.V.: Recent advances in microscale pumping technologies: a review and evaluation. Microfluid. Nanofluid. **5**, 145–174 (2008)

97. Woias, P.: Micropumps—past, progress and future prospects. Sens. Actuators B Chem. **105**, 28–38 (2005)

98. Au, A.K., Lai, H., Utela, B.R., Folch, A.: Microvalves and micropumps for BioMEMS. Micromachines **2**, 179–220 (2011)

99. Yokota, S.: A review on micropumps from the viewpoint of volumetric power density. Mech. Eng. Rev. **1**, 1–14 (2014)

100. Li, H., Liu, J., Li, K., Liu, Y.: A review of recent studies on piezoelectric pumps and their applications. Mech. Syst. Signal Process. **151**, 107393 (2021)

101. Nguyen, N.-T., Huang, X., Chuan, T.K.: MEMS-micropumps: a review. J. Fluids Eng. **124**, 384–392 (2002)

102. Singhal, V., Garimella, S.V., Raman, A.: Microscale pumping technologies for microchannel cooling systems. Appl. Mech. Rev. **57**, 191–221 (2004)

103. Tsai, N.-C., Sue, C.-Y.: Review of MEMS-based drug delivery and dosing systems. Sens. Actuators A Phys. **134**, 555–564 (2007)

104. Saffman, P.G., Taylor, G.I.: The penetration of a fluid into a porous medium or Hele-Shaw cell containing a more viscous liquid. Proc. R. Soc. A Math. Phys. Eng. Sci. **245**, 312–329 (1958)

105. Nase, J., Lindner, A., Creton, C.: Pattern formation during deformation of a confined viscoelastic layer: from a viscous liquid to a soft elastic solid. Phys. Rev. Lett. **101**, 074503 (2008)

106. Cheon, J., Kim, S.: Intermediate layer-based bonding techniques for polydimethylsiloxane/digital light processing 3D-printed microfluidic devices. J. Micromech. Microeng. **29**, 095005 (2019)

107. Thompson, C.S., Abate, A.R.: Adhesive-based bonding technique for PDMS microfluidic devices. Lab Chip **13**, 632–635 (2013)

108. Wang, P., Chen, Z., Chang, H.-C.: A new electro-osmotic pump based on silica monoliths. Sens. Actuators B Chem. **113**, 500–509 (2006)

109. Brask, A., Kutter, J.P., Bruus, H.: Long-term stable electroosmotic pump with ion exchange membranes. Lab Chip **5**, 730–738 (2005)

110. Saren, A., Smith, A., Ullakko, K.: Integratable magnetic shape memory micropump for high-pressure, precision microfluidic applications. Microfluid. Nanofluid. **22**, 1–10 (2018)

111. Skafte-Pedersen, P., Sabourin, D., Dufva, M., Snakenborg, D.: Multi-channel peristaltic pump for microfluidic applications featuring monolithic PDMS inlay. Lab Chip **9**, 3003–3006 (2009)

112. Zeng, S., Chen, C.-H., Mikkelsen, J.C., Jr., Santiago, J.G.: Fabrication and characterization of electroosmotic micropumps. Sens. Actuators B Chem. **79**, 107–114 (2001)

113. Chen, Z., Wang, P., Chang, H.-C.: An electro-osmotic micropump based on monolithic silica for micro-flow analyses and electro-sprays. Anal. Bioanal. Chem. **382**, 817–824 (2005)

114. Chen, L., Guan, Y., Ma, J., Luo, G., Liu, K.: Application of a high-pressure electro-osmotic pump using nanometer silica in capillary liquid chromatography. J. Chromatogr. A **1064**, 19–24 (2005)

115. Borowsky, J., Lu, Q., Collins, G.E.: High pressure electroosmotic pump based on a packed bed planar microchip. Sens. Actuators B Chem. **131**, 333–339 (2008)

116. Paul, P.H., Arnold, D.W., Rakestraw, D.J.: Micro Total Analysis Systems' 98, pp. 49–52. Springer, Berlin (1998)

117. Bodén, R., Hjort, K., Schweitz, J.-Å., Simu, U.: A metallic micropump for high-pressure microfluidics. J. Micromech. Microeng. **18**, 115009 (2008)

118. Svensson, S., Sharma, G., Ogden, S., Hjort, K., Klintberg, L.: High-pressure peristaltic membrane micropump with temperature control. J. Microelectromech. Syst. **19**, 1462–1469 (2010)

119. Bodén, R., Ogden, S., Hjort, K.: Microdispenser with continuous flow and selectable target volume for microfluidic high-pressure applications. J. Microelectromech. Syst. **23**, 452–458 (2013)